# Shape control of deformable charge-patterned nanoparticles

Fanbo Sun <sup>1</sup>, Nicholas E. Brunk <sup>2</sup>, <sup>2,3</sup> and Vikram Jadhao <sup>1</sup>,\*

Intelligent Systems Engineering, Indiana University, Bloomington, Indiana 47408, USA

Wolfram Research, Champaign, Illinois 61820, USA

American Regent, Norristown, Pennsylvania 19403, USA

(Received 23 June 2022; accepted 5 December 2022; published 10 January 2023)

Deformable nanoparticles (NPs) offer unprecedented opportunities as dynamic building blocks that can spontaneously reconfigure during assembly in response to environmental cues. Designing reconfigurable materials based on deformable NPs hinges on an understanding of the shapes that can be engineered in these NPs. We solve for the low-energy shapes of charge-patterned deformable NPs by using molecular dynamics-based simulated annealing to minimize a coarse-grained model Hamiltonian characterized with NP elastic and electrostatic energies subject to a volume constraint. We show that deformable spherical NPs of radius 50 nm whose surface is tailored with octahedrally distributed charged patches and double-cap charged patches adapt their shape differently in response to changes in surface charge coverage and ionic strength. We find shape transitions to rounded octahedra, faceted octahedra, faceted bowls, oblate spheroids, spherocylinders, dented beans, and dimpled rounded bowls. We demonstrate that similar shape transitions can be achieved in deformable NPs of different sizes. The effects of counterion condensation on the free-energetic drive associated with the observed deformations are examined via Manning model calculations that utilize simulation-derived estimates for the NP Coulomb energy under salt-free conditions. The charge-pattern-based shape control of deformable NPs has implications for the design of responsive nanocontainers and for assembling reconfigurable materials whose functionality hinges on the shape-shifting properties of their nanoscale building blocks.

#### DOI: 10.1103/PhysRevE.107.014502

## I. INTRODUCTION

Understanding the generation and control of particle shape at the nanoscale is important in designing materials via assembly engineering strategies. There is a keen interest in how self-assembly is affected by nanoscale building blocks that spontaneously reconfigure during assembly in response to environmental cues [1–8]. This dynamic dimension enables unique structural organizations via otherwise inaccessible assembly pathways, broadening assembly engineering approaches aimed at designing reconfigurable materials.

Deformable nanoparticles (NPs) fabricated using polymeric materials are important examples of dynamic nanoscale building blocks [9–12]. These NPs are also being investigated for designing stimuli-responsive nanocontainers in therapeutic applications [13–15], where studies demonstrate that the cellular uptake of nanocarriers is affected by their shape, size, charge, and deformability [16–19]. Many techniques have been developed to synthesize deformable NPs, including methods where electrostatic interactions play a key role in inducing shape changes via pH or ionic strength modulation [9,20–24]. Advances in nanotechnology have enabled the synthesis of charge-patterned NPs [12,25–28] and expanded the use of electro-

static control to induce changes in NP assembly behavior [29–31].

Designing reconfigurable materials based on deformable NPs hinges on an understanding of the energetically favored shapes these NPs can adopt. Theoretical efforts have focused on understanding shape transitions in uncharged elastic shells, whose deformation is driven by topological defects, compression, or magnetic forces [32–35]. Shapes of homogeneously charged nanostructures have also been investigated [36–39]. Recently, we considered a specific class of deformable NPs, those whose surface is tailored with charged patches [40]. Computational studies of deformations of patchy, flexible NPs have been largely limited to the use of elastic inhomogeneities to drive shape transitions, for example, into regular polyhedra, buckled conformations, and collapsed bowl-like structures [41–46]. In Ref. [40], we demonstrated the capacity to electrostatically control the shape of deformable NPs in aqueous solutions over a broad range of salt concentrations via the synthesis of surface charge patterns. Using simulations, we showed that hollow, deformable spherical NPs of radius R = 20 nm tailored with surface charge patterns such as Janus patches, stripes, and polyhedrally distributed patches adapt their shape differently in response to changes in patterns and salt concentration over 0.05-20 mM. Driven by the lowering of the NP electrostatic energy, we found volume-preserving shape transitions to hemispheres, spinning tops, capsules, flattened bowls, disks, and tetrahedrally shaped particles.

Here we extend the investigation to probe the low-energy shapes of deformable NPs of larger sizes that are designed

<sup>\*</sup>vjadhao@iu.edu

with two new types of surface charge patterns: octahedrally distributed patches and double-cap patterns, the latter representing two identical charged spherical caps at the opposite poles of a spherical NP. Using molecular dynamics (MD) based simulated annealing, we solve for the low-energy shapes of these charge-patterned deformable NPs by minimizing a coarse-grained model Hamiltonian characterized with elastic and electrostatic energies subject to a volume constraint. Our simulations show that spherical NPs of radius R = 50 nm, bending modulus  $\kappa_b = 15k_BT$ , and stretching modulus  $\kappa_s = 1500k_BT$  whose surface is tailored with octahedrally distributed patches characterized with charge density  $\sigma \approx 0.08e/\text{nm}^2$  deform into rounded and faceted octahedra, faceted bowls, and rounded bowls in response to changes in surface charge coverage and salt concentration over 0.01-10 mM. The same NPs when designed with double-cap patches deform into oblate spheroids, spherocylinders, dented beanshaped structures, and rounded bowls in response to similar changes in charge coverage and salt concentration. The elastic moduli of NPs are 3× more rigid compared to those considered previously [40], and correspond to three-dimensional (3D) Young's modulus in the 10-100 kPa range, which is central to the experimental studies of flexible NPs made using polymeric gels [10,11]. We show that by tuning the NP design attributes and solution conditions, similar shape transitions can be achieved in deformable NPs of different sizes characterized with R = 30 and 75 nm.

All shape transitions are driven by the competition between the electrostatic and elastic energies characterizing the NP, which is tuned by changing the NP attributes and solution conditions. The deformations preserve the NP volume and exhibit an overall reduction in the NP total energy and an increase in the NP surface area. The elastic and electrostatic energy densities on the surface of the deformed charge-patterned NPs are coupled to the NP shape. The effects of counterion condensation are examined by assessing the free-energetic drive for fully charged spherical NPs, which experience the highest ion condensation, to deform into rounded bowl-shaped NPs for low salt concentrations. We introduce a Manning model that utilizes simulation-derived estimates for the NP Coulomb energy to enable the extraction of effective charge and free energy for NPs of arbitrary shapes under salt-free conditions. Manning model calculations show that the deformation into bowl-shaped NPs is free-energetically favorable in many cases for a wide range of NP concentration or volume packing fraction  $\eta$  in the range  $10^{-13} < \eta < 10^{-2}$ , despite high counterion condensation at larger  $\eta$ . In some cases involving higher  $\eta$ , where significant counterion condensation inhibits deformation, we show that the free-energetic drive to deform can be restored by synthesizing softer NPs and modulating the total surface charge.

## II. MODELS AND SIMULATION METHODS

The model NPs are initialized as hollow spheres of radius R. Following our earlier work, the NP surface is modeled with a set of discrete points forming a mesh of  $N_v$  vertices, constituting  $N_e$  edges and  $N_f$  triangular faces. Bending modulus  $\kappa_b$  and stretching constant  $\kappa_s = k_s R^2$ , where  $k_s$  is the spring constant, are introduced to effectively account for the

intermolecular short-range elastic interactions that resist deformation. Bending energy depends on the normals  $\vec{n}_{l_1}$  and  $\vec{n}_{l_2}$ to the faces opposite each edge l and is measured relative to the planar conformation, which is assigned the lowest (zero) bending energy. Stretching energy between neighboring pair of vertices is measured relative to the initial spherical conformation which has the lowest (zero) stretching energy. The two-dimensional (2D) elastic parameters  $\kappa_b$  and  $\kappa_s$  are chosen in a regime where the uncharged NP is spherical at equilibrium. The parameter values are inspired by experiments that demonstrate significant deformation in hydrogel NPs characterized with 3D Young's modulus in the 10-100 kPa range [10,11,47–49]. We only consider deformations that preserve the NP's total volume, which is constrained to that of the initial spherical NP. The volume constraint can be representative of closed vesicles that do not exchange significant matter with their environment and is motivated by experimental studies where the preservation of the amount of cargo encapsulated within the NP is desired across different shapes [14,50].

The surface charge patterns are restricted to designed patches exhibiting charges of only one sign. The process of designing the surface of a spherical NP with charged patches begins by assigning each vertex associated with the charged patch a charge proportional to its area. Because a sphere cannot be uniformly triangulated, the mesh of  $N_v$  vertices has some vertices with different areas (defects). To ensure that the NP deformation is not resulting from these defects, the charges on the vertices associated with the charged patches are randomly shuffled. This process produces small variations in the vertex charges associated with the patchy regions, and generates approximately the same surface charge per patch. The nonuniform distribution of vertex charges associated with a patch does not play any significant role in determining the low-energy shapes. The charged patches on the surface of the spherical NPs designed via the above process exhibit an approximately uniform surface charge density  $\sigma$ . During the deformation of NPs,  $\sigma$  changes, often decreasing due to the increase in the area associated with the patchy regions. Both undeformed and deformed NPs exhibit the same vertex charge distribution and total surface charge.

Two sets of charge patterns are considered: octahedrally distributed patches and double-cap patches. Electrostatic interactions between charged vertices are included via a screened Coulomb potential with screening length  $\lambda = 1/\sqrt{8\pi l_B I}$  representing the effects of mobile ions in the solution inhabiting the NP, where  $l_B$  is Bjerrum length and I is the ionic strength of the solution. For the monovalent electrolyte in an aqueous environment considered in this work,  $l_B \approx 0.7$  nm and  $I = c_s$ , where  $c_s$  is the salt concentration.

Following Ref. [40], we write the Hamiltonian  $\mathcal{H}$  describing the model NP system in units of  $k_BT$  as:

$$\mathcal{H} = \frac{\kappa_b}{2} \sum_{l=1}^{N_e} |\vec{n}_{l_1} - \vec{n}_{l_2}|^2 + \frac{\kappa_s}{2R^2} \sum_{l=1}^{N_e} (|\vec{r}_{l_1} - \vec{r}_{l_2}| - a_l)^2 + \frac{l_B}{2} \sum_{i=1}^{i=N_v} \sum_{j\neq i}^{j=N_v} q_i q_j e^{-|\vec{r}_i - \vec{r}_j|/\lambda} / |\vec{r}_i - \vec{r}_j|,$$
(1)

where the first, second, and third terms are the total bending, stretching, and electrostatic energy, respectively.  $\vec{r}_{l_1}$  and  $\vec{r}_{l_2}$  are the position vectors of the vertices corresponding to edge l with equilibrium length  $a_l$ ,  $\vec{r}_i$  denotes the position vector of vertex i, and  $q_i$  is the charge associated with this vertex.  $\mathscr{H}$  is extended to include a global volume constraint term to preserve the entire volume of the initial spherical NP during the deformation process. The volume constraint is imposed as a linear term:  $\sum_{k \in N_f} (V_k - V_{k_0})$ , where  $V_k$  is the volume subtended by the kth face of the discretized NP surface and  $V_{k_0}$  is its initial volume. In the limit of large total number of faces  $N_f$ , the NP volume becomes  $(4/3)\pi R^3$ .

The Hamiltonian  ${\mathscr H}$  is a function of the position vectors of the vertices, which parametrize the shape of the NP. The low-energy shapes correspond to the minimum of  $\mathcal{H}$ subject to the volume constraint. The constrained minimization is performed using an MD-based simulated annealing procedure [51] described in our earlier work [36,38,40]. To summarize, we assign the vertices a kinetic energy  $\mathcal{K} =$  $\sum_{i} (1/2) \mu |\vec{r}_{i}|^{2}$  and write the Lagrangian  $\mathcal{L} = \mathcal{K} - \mathcal{H}$ .  $\mu$  is a mass term associated with the vertices that determines the simulation timestep, and  $\vec{r}_i$  denotes the velocity of vertex *i*. The vertex positions are evolved using the equations of motion derived from  $\mathcal{L}$ , which are appropriately augmented via the SHAKE-RATTLE algorithm to preserve the NP volume at each simulation step [52]. The simulation begins at a high fictitious temperature to enable the NP surface to deform by exploring the energy landscape, after which kinetic energy is slowly removed from the system regulated via a Nosé-Hoover thermostat. This allows a gradual convergence on the fluctuating shapes of low energy. The NP shape evolution can get trapped in a metastable state in simulations. As a result, the low-energy shapes found in simulations are not necessarily the true ground states of  $\mathcal{H}$  but modes that describe the characteristic NP behavior as it approaches the true ground state.

The low-energy NP shapes are determined by the charge pattern, salt concentration, elastic moduli, and NP size. The NPs considered in this work are larger and more rigid compared to our previous paper [40]. Converged results were obtained with a constant mesh size of  $N_v = 9992$  vertices. Larger mesh sizes (e.g.,  $N_v = 13\,392,\,17\,292$ ) produced similar shapes, areas, and energies as those obtained with  $N_v = 9992$  vertices. Over 500 simulations, each taking  $\approx 20$  hours to finish using 4 nodes and 24 processors per node, were run to obtain the data necessary to establish the pattern-shape links shown in Sec. III.

## III. RESULTS AND DISCUSSION

## A. Shape transitions

We first show the results for the low-energy conformations of NPs of volume  $\approx (4/3)\pi\,50^3$  nm³ whose surface is tailored with octahedrally distributed charged patches, i.e., six identical charged patches centered around the vertices of an inscribed octahedron. All NPs are initialized as spheres designed with these six charged patches, the vertices associated with each patch have approximately the same surface charge density  $\sigma \approx 0.08e/\text{nm}^2$ . The surface charge pattern

is characterized by the fractional surface charge coverage parameter p defined as the fraction of the total area of the spherical NP that is charged. Increasing p produces NPs of larger charge per patch and larger total surface charge, which scales as pQ, where  $Q \approx 4\pi R^2 \sigma \approx 2513e$  is the total surface charge associated with a fully charged NP. The NPs have a bending modulus  $\kappa_b = 15k_BT$  and a stretching modulus  $\kappa_s = 1500k_BT$ , which correspond to a Föppl von Kármán number  $\gamma = 100$ . For these elastic parameters, the low-energy shape of an uncharged NP (p = 0) is a sphere. All NPs are in an aqueous solution.

Figure 1 shows the low-energy NP shape for different charge coverage parameters p and salt concentrations  $c_s$ , with p increasing from bottom to top as p =0.25, 0.5, 0.75, 1 and  $c_s$  increasing from left to right as  $c_s =$ 0.01, 0.05, 0.1, 0.5, 1, 5 mM. The nonuniform color on the surface of the patchy regions indicates the small variations in the charge per vertex resulting from the mesh used to triangulate the NP surface. For  $c_s = 5$  mM, NPs assume a similar spherelike shape for different p. However, for  $c_s \lesssim 5$ mM, NPs patterned with octahedrally distributed patches of different charge coverage parameters adapt their shape differently in response to the reduction in salt concentration. For p = 0.25, shape transitions to rounded octahedra are observed as  $c_s$  is decreased from 1 to 0.01 mM. The octahedra become less round, and increasingly more faceted, with decreasing  $c_s$ . For p = 0.5, transitions to rounded, faceted, and concave octahedral particles are observed within the same range of  $c_s$ . For p = 0.75, the NP exhibits shape transitions from sphere to rounded octahedra to faceted bowls, which are characterized by the inward buckling of the uncharged region between the two charged patches. As the fully charged limit is approached with p = 1, transitions to rounded bowls of varying depth are observed, which have been reported in our earlier work [36,38,40]. Further, for a fixed  $c_s \lesssim 1$  mM, NP shape can be modulated by increasing p. For example, at  $c_s = 0.5$  mM, the NP deforms from rounded octahedron to faceted octahedron to faceted and rounded bowls as p is increased from 0.25 to 1.

We next discuss the low-energy shapes of NPs whose surface is tailored with two identical charged patches placed at diametrically opposite ends of the sphere. Both charged caps have the same area and charge density  $\sigma \approx 0.08e/\text{nm}^2$ . These double-cap patterns are also characterized by the fractional surface charge coverage parameter p. Other parameters such as the NP size, elastic moduli, and solution conditions are the same as those for NPs designed with octahedrally distributed patches.

Figure 2 shows the low-energy NP shape for different p and  $c_s$ , with p increasing from bottom to top as p = 0.25, 0.40, 0.50, 0.75, and  $c_s$  increasing from left to right as  $c_s = 0.01, 0.05, 0.1, 0.5, 1, 5$  mM. For  $c_s = 5$  mM, NPs assume a similar spherelike shape for all p. However, for  $c_s \lesssim 5$  mM, NPs patterned with double-cap patterns of different p values adapt their shape differently in response to the reduction in  $c_s$ . For p = 0.25, transitions to a variety of oblate spheroidal structures are observed as  $c_s$  is decreased from 1 to 0.01 mM. For p = 0.4, the NP exhibits transitions to oblate spheroids and spherocylinders. The spherocylinders are characterized with an uncharged cylindrically shaped region and two charged spherical end-caps. For p = 0.5, transitions

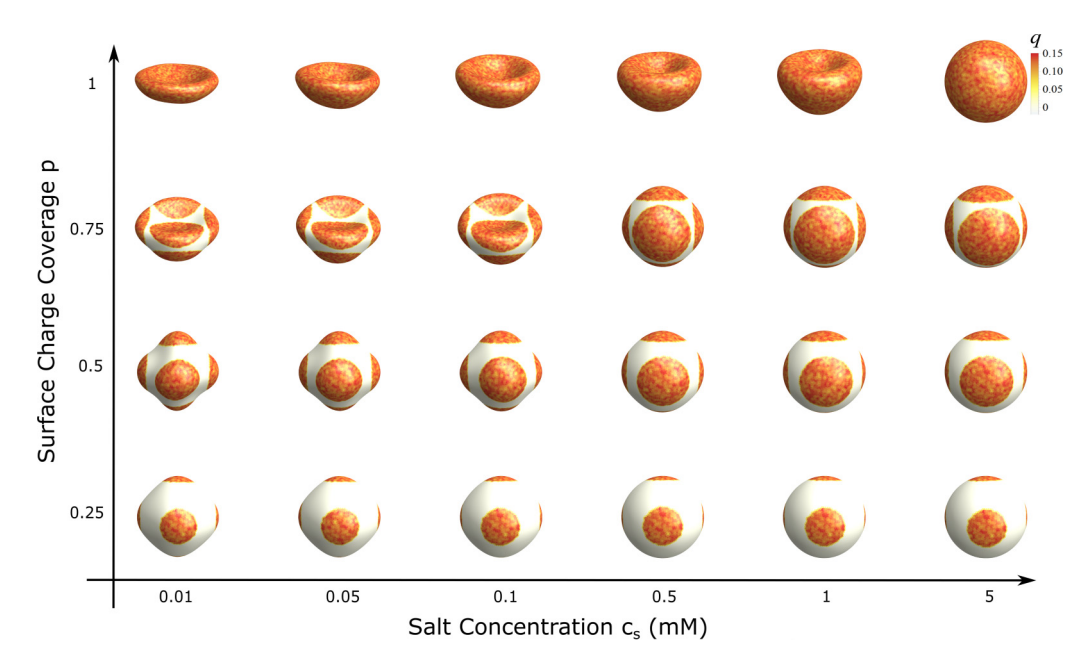


FIG. 1. Snapshots of low-energy shapes of deformable NPs patterned with octahedrally distributed charged patches (colored in orange). The fractional surface charge coverage p increases from bottom to top as 0.25, 0.50, 0.75, 1.0 and the salt concentration  $c_s$  increases from left to right as 0.01, 0.05, 0.1, 0.5, 1, 5 mM. All NPs have the same volume  $\approx (4/3)\pi 50^3$  nm<sup>3</sup> and elastic moduli  $\kappa_b = 15k_BT$ ,  $\kappa_s = 1500k_BT$ . NPs are characterized with a surface charge of pQ, where  $Q \approx 2513e$  is the total surface charge associated with a fully charged NP. The color bar indicates the charge in units of e associated with the vertices discretizing the NP surface. Shifting the pattern changes the sequence of low-energy shapes as a function of  $c_s$ . NPs characterized with p = 0.25 and 0.5 deform into rounded and faceted octahedra. NPs characterized with p = 0.75 and p = 1 deform into faceted and rounded bowls.

from sphere to spherocylinders to dented beanlike structures are observed. The depth of the dents changes with  $c_s$ . For p = 0.75, the NP transitions from spherelike shapes to more

flattened beanlike structures, the flattening increasing with decreasing  $c_s$ . In the uniformly charged limit (p = 1), transitions to bowl conformations shown in Fig. 1 are recovered. For a

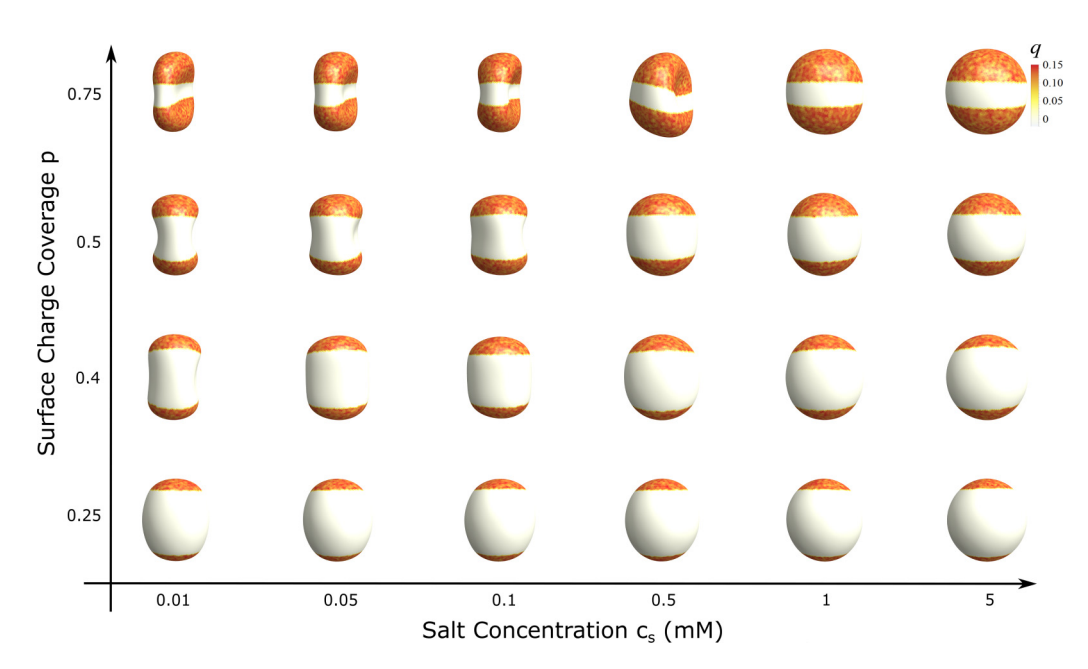


FIG. 2. Snapshots of low-energy shapes of deformable NPs patterned with double-cap charged patches (colored in orange). The charge coverage p increases from bottom to top as 0.25, 0.40, 0.5, 0.75 and the salt concentration  $c_s$  increases from left to right as 0.01, 0.05, 0.1, 0.5, 1, 5 mM. All NPs have the same volume  $\approx (4/3)\pi 50^3$  nm<sup>3</sup> and elastic moduli  $\kappa_b = 15k_BT$ ,  $\kappa_s = 1500k_BT$ . NPs are characterized with a surface charge of pQ, where  $Q \approx 2513e$  is the total surface charge associated with a fully charged NP. The color bar indicates the charge in units of e associated with the vertices discretizing the NP surface. Shifting the pattern changes the low-energy shapes as a function of  $c_s$ . NPs deform into oblate spheroids, spherocylinders, and dented bean-shaped structures.

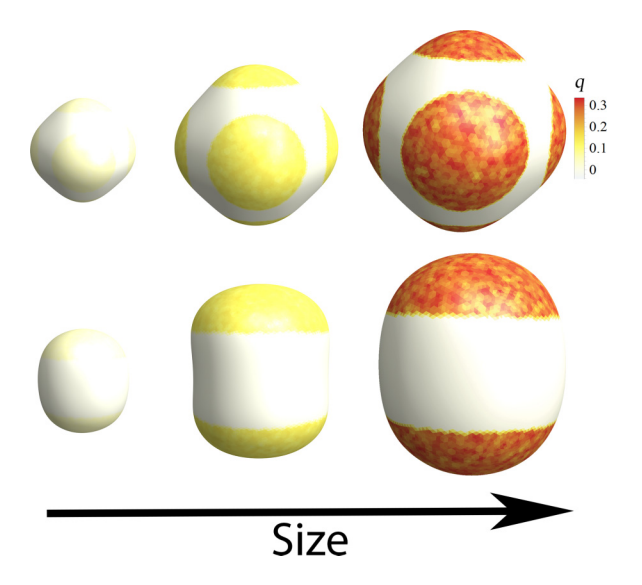


FIG. 3. Similar shapes can be realized in NPs of different sizes by tuning the NP design attributes and solution conditions. Spherical NPs of radius R=30, 50, and 75 nm designed with octahedrally distributed (top row) and double-cap (bottom row) charged patches characterized by coverage parameter p=0.5 transform into differently sized octahedra and spherocylinders. The smallest NPs have elastic moduli  $\kappa_b=10k_BT$ ,  $\kappa_s=1000k_BT$ , while the two larger sets of NPs have  $\kappa_b=15k_BT$ ,  $\kappa_s=1500k_BT$ . The total surface charge Q and salt concentration  $c_s$  of the solution increase with size as Q=453, 1256, 2827e and  $c_s=0.01$ , 0.2, 1 mM. The color bar indicates the charge in units of e associated with the vertices discretizing the NP surface.

fixed  $c_s \lesssim 1$  mM, NP shape can be modulated by increasing p. For example, at  $c_s = 0.1$  mM, the NP deforms from oblate spheroid to spherocylinder to rounded and flattened beans as p is increased from 0.25 to 0.75.

Changing NP elasticity can alter the gallery of low-energy shapes of charge-patterned deformable NPs. For example, when the stretching modulus is decreased from  $\kappa_s = 1500k_BT$  to  $375k_BT$  (keeping all other NP features the same as above), NPs tailored with octahedrally distributed charged patches exhibit different shape transitions. At a salt concentration of  $c_s = 1$  mM, these softer NPs exhibit shape transitions to rounded cubes, faceted plates, and flattened bowls as the charge coverage p is increased from 0.25 to 1 (Fig. 8 in the Appendix).

The low-energy shapes shown in Figs. 1 and 2 can be realized in NPs of different sizes by moderately tuning the NP design attributes and solution conditions. For example, Fig. 3 illustrates that spherical NPs of radius R = 30, 50, and 75 nm designed with octahedrally distributed patches and double-cap patterns characterized by charge coverage p = 0.5 transform into differently sized octahedra (top row) and spherocylinders (bottom row), respectively. The shapes for NPs characterized with R = 50 nm are realized for the same NPs considered above at  $c_s = 0.2$  mM. Larger NPs characterized with R = 75 nm exhibit similar shapes at the same elastic moduli for the total surface charge Q = 2827e and  $c_s = 1$  mM. NPs characterized with R = 30 nm exhibit similar shapes at  $c_s = 0.01$  mM when their elastic moduli are

reduced to  $\kappa_b = 10k_BT$  and  $\kappa_s = 1000k_BT$ , and Q is decreased to 453e.

#### B. Quantifying shape transitions

The links between the surface charge patterns and the low-energy NP shapes can be quantified by analyzing the changes in the energy and the area of the NPs relative to the initial spherical conformation. Figure 4 shows the total energy difference  $\Delta \mathscr{H} = \mathscr{H} - \mathscr{H}_s$  and normalized area  $A/A_s$  (inset) vs salt concentration  $c_s$  associated with deformed NPs patterned with octahedrally distributed patches (a) and double-cap patches (c).  $\mathcal{H}$  and A denote, respectively, the total energy and area of the deformed NP.  $\mathcal{H}_s$  and  $A_s$  denote, respectively, the total energy and area of the associated initial spherical NP of radius R = 50 nm. For both sets of surface charge patterns,  $\Delta \mathcal{H} \approx 0$  and  $A/A_s \approx 1$  at  $c_s = 5$  mM for different charge coverage parameters p. Corresponding lowenergy NP shapes (rightmost column in Figs. 1 and 2) are indeed nearly spherical. As  $c_s$  is lowered,  $\Delta \mathcal{H}$  becomes more negative and  $A/A_s$  increases for all p. These trends signal that the shape transitions seen in Figs. 1 and 2 are accompanied by a decrease in the total energy and an increase in the NP area relative to the initial, undeformed spherical NP.

It is informative to examine the electrostatic and elastic energy components of the total Hamiltonian  $\mathcal{H}$  describing the deformed NPs. The elastic energy is defined as the sum of the NP bending and stretching energy terms in Eq. (1). Figure 4 shows the electrostatic energy difference  $\Delta \mathcal{U} = \mathcal{U} - \mathcal{U}_s$  and the elastic energy difference  $\Delta \mathcal{H}^{\text{elastic}} = \mathcal{H}^{\text{elastic}} - \mathcal{H}^{\text{elastic}}_{s}$ (inset) vs  $c_s$  for deformed NPs patterned with octahedrally distributed patches (b) and double-cap patches (d).  $\mathscr U$  and  $\mathscr{H}^{\text{elastic}}$  denote, respectively, the electrostatic energy and elastic energy of the deformed NP.  $\mathcal{U}_s$  and  $\mathcal{H}_s^{\text{elastic}}$  denote, respectively, the electrostatic energy and elastic energy of the initial spherical NP of radius R = 50 nm. In all cases,  $\Delta \mathcal{U} <$ 0 and  $\Delta \mathcal{H}_s^{\text{elastic}} > 0$ , indicating that the deformation is driven by the lowering of the electrostatic energy and is associated with a rise in the elastic energy. This competition between the electrostatic and elastic energies sets an effective area for the NP, which in conjunction with the volume constraint, determines the resulting NP shape.

Figure 5 shows the distribution of local elastic energy density on the NP surface for a representative set of deformed NPs. The elastic energy density is computed as the sum of the bending and stretching energies associated with the finite elements discretizing the NP surface. The elastic energy density distribution is inhomogeneous and exhibits a coupling to the NP shape. Similarly, the electrostatic energy density on the NP surface is inhomogeneous and couples strongly to the surface charge pattern (see Fig. 9 in the Appendix). NPs tailored with octahedrally distributed charged patches characterized by p = 0.25 (a) and p = 0.5 (b) deform into faceted octahedral shapes that exhibit larger elastic energy density at the sites of the charged patches compared to the uncharged regions. When these charge-patterned NPs are characterized by p = 0.75 (c), they deform into faceted bowls and we observe higher elastic energy density along the rim of the bowl. NPs tailored with double-cap charged patches characterized by p = 0.25 (d) deform into oblate spheroidal shells and show higher elastic

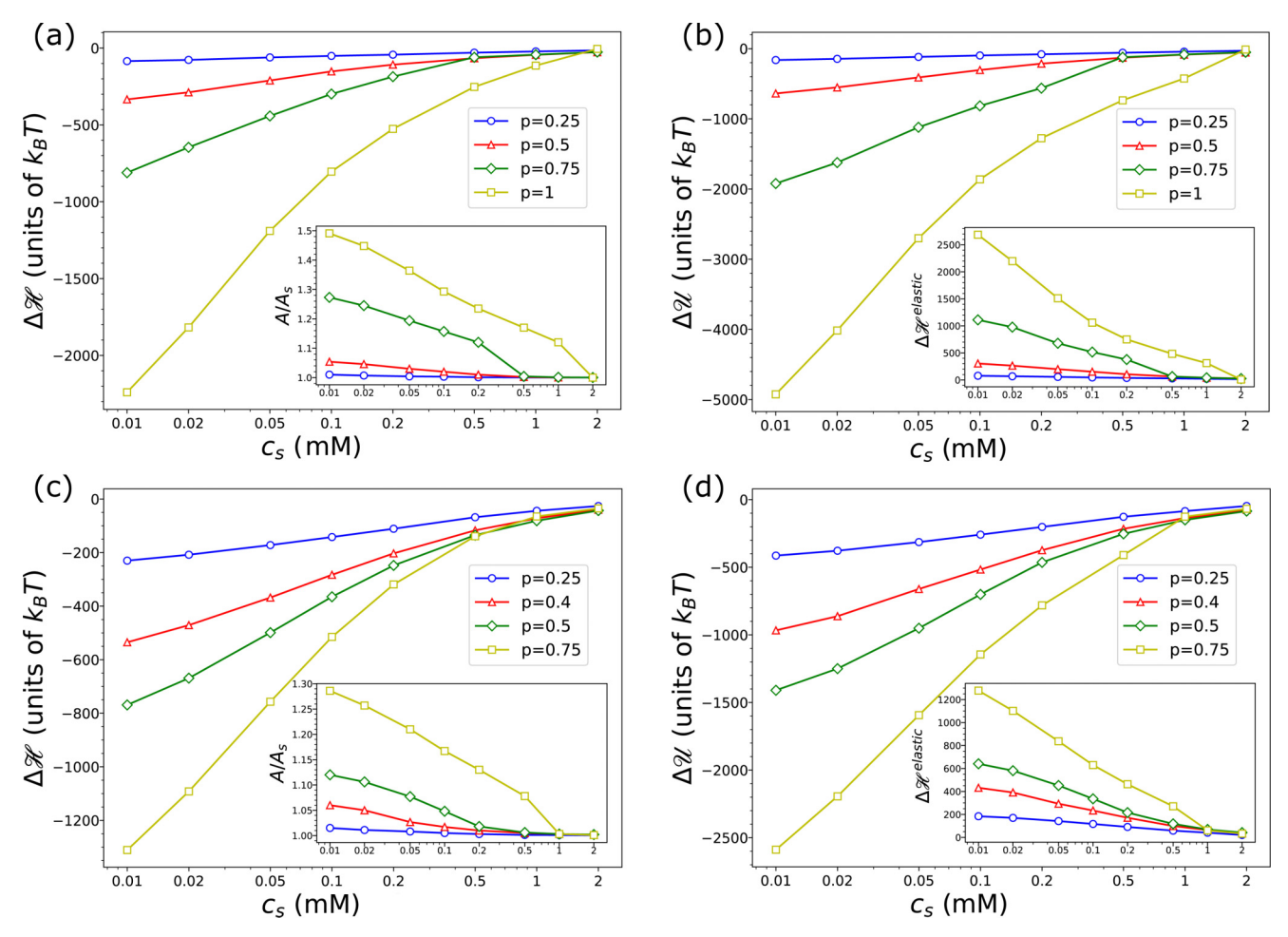


FIG. 4. Total energy  $\Delta \mathcal{H}$  and surface area  $A/A_s$  (inset) of deformed NPs relative to that of the initial spherical NPs of radius R=50 nm vs salt concentration  $c_s$  for NPs patterned with octahedrally distributed patches (a) and double-cap patches (c) characterized by charge coverage p noted in the legend. Associated electrostatic energy  $\Delta \mathcal{H}$  and elastic energy  $\Delta \mathcal{H}$  elastic (inset) in units of  $k_B T$  of deformed NPs relative to that of the initial spherical NPs are shown for NPs patterned with octahedrally distributed patches (b) and double-cap patches (d). Results correspond to NP shapes shown in Figs. 1 and 2. Shape transitions are accompanied by a decrease in the total energy and electrostatic energy, and an increase in the area and elastic energy relative to the spherical NP.

energy within the two deformed end-caps compared to the undeformed, central region. When these charge-patterned NPs are characterized by p=0.4 (e) and p=0.5 (f), they deform into spherocylinders and beans, respectively, and accordingly we observe higher elastic energy within the end caps as well as the stretched central region of the NP surface.

## C. Ion condensation effects

In the charge-patterned deformable NP model described by the Hamiltonian  $\mathcal{H}$ , all charged patches have the same surface charge density  $\sigma$ . However, the NP surface charge varies with the pattern and is largest for the fully charged NP. Under dilute conditions, i.e., small NP packing fraction  $\eta$ , we can utilize the net surface charge and the associated total energy difference  $\Delta\mathcal{H}$  to assess the feasibility of shape transitions. As  $\eta$  increases, counterion condensation on the NP surface can become significant and the free-energy difference between the deformed and undeformed NPs becomes a more appropriate metric to assess the stability of shape transitions.

In our earlier work, we used MD simulations of monovalent counterions near undeformed and deformed NPs to evaluate the fraction of counterions that condense on the NP surface under no salt conditions  $(c_s \rightarrow 0)$  for NPs characterized with R=20 nm,  $\sigma=0.12e/\mathrm{nm}^2$ , and elastic moduli  $\kappa_b = 5k_BT$ ,  $\kappa_s = 125k_BT$  [38,40]. For high  $\eta = 10^{-3}$  and  $10^{-2}$ , simulations showed that among all patchy NPs, ion condensation is most severe for NPs whose surfaces are fully charged  $(p \rightarrow 1)$ . In this limit, simulated annealing procedure predicted disklike conformations as low-energy shapes of NPs for low  $c_s \sim 1$  mM. By approximating these structures as uniformly charged oblate spheroidal shells, we evaluated the NP Coulomb energy analytically and performed meanfield calculations under salt-free conditions using a two-state Manning model to calculate the NP effective charge and free energy. Manning model calculations reproduced the effective charge estimated by the MD simulations and showed that the difference between the free energy of the disklike NP and the initial undeformed sphere is negative by over  $80k_BT$  for  $10^{-12} < \eta < 10^{-2}$ , implying sphere-to-disk transitions were free-energetically favorable in the event of ion condensation.

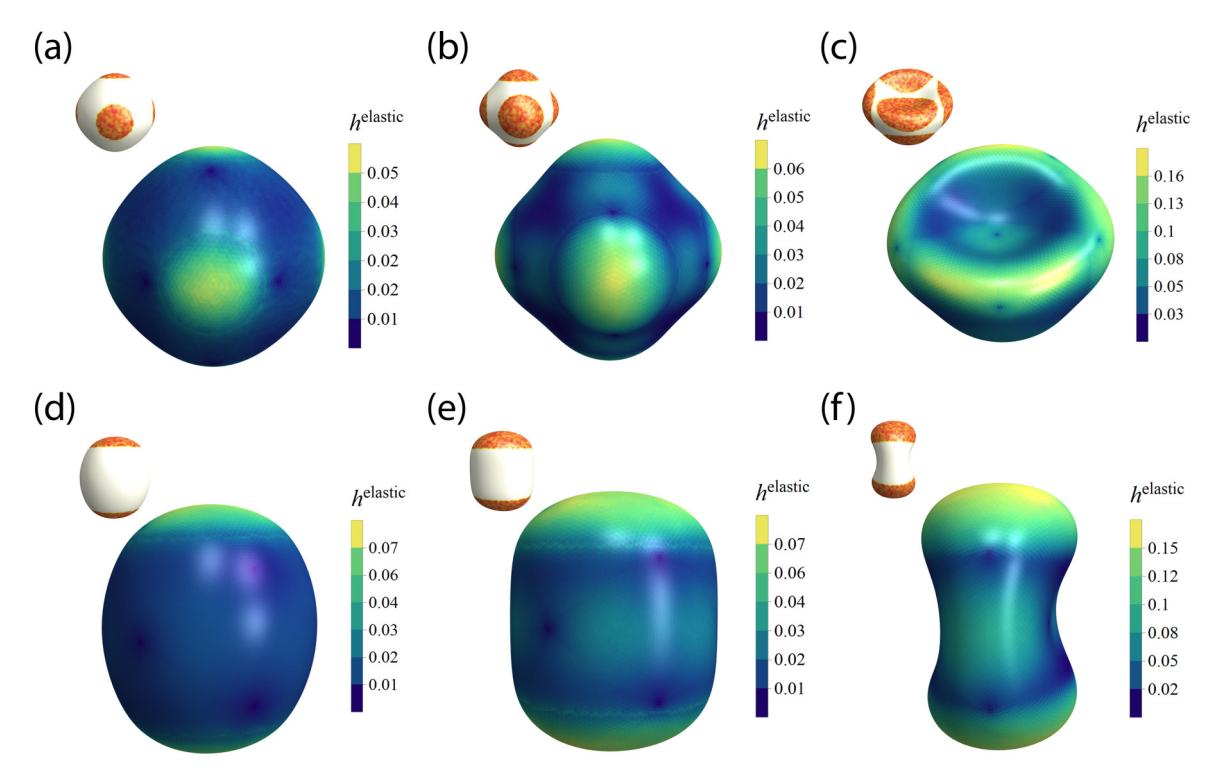


FIG. 5. The elastic energy density  $h^{\text{elastic}}$  in units of  $k_BT$  for a representative set of deformed NPs of volume  $(4/3)\pi 50^3$  nm<sup>3</sup> tailored with octahedrally distributed charged patches characterized by charge coverage p = 0.25 (a), p = 0.5 (b), and p = 0.75 (c), and double-cap patterns characterized by p = 0.25 (d), p = 0.4 (e), and p = 0.5 (f). The top left image in each case shows the associated surface charge pattern. The elastic energy density is inhomogeneous and exhibits a coupling to the shape of the charge-patterned NP.

Motivated by these studies, we examine the effects of counterion condensation on the deformation of fully charged spherical NPs characterized with R = 50 nm,  $\kappa_b = 15k_BT$ ,  $\kappa_s = 1500k_BT$ , and  $\sigma = 0.08e/\text{nm}^2$ , which corresponds to a total surface charge Q = 2513e. For these larger NPs, MD simulations are computationally expensive due to the associated larger number of mesh points needed to ensure stable ion-NP steric interactions and because of the prohibitively long equilibration timescales for counterion dynamics within the large volume corresponding to the bulk region. The fully charged limit  $p \rightarrow 1$  yields bowls as low-energy shapes of these NPs for  $c_s \lesssim 1$  mM (top row in Fig. 1). An analytical expression for the Coulomb energy of a bowl-shaped shell is not available. However, we show that by utilizing simulationbased estimates for the Coulomb energy of the bowl-shaped NPs in a Manning model, the free-energetic drive for sphereto-bowl shape transitions can be examined under salt-free conditions.

We consider a single NP in the center of a spherical Wigner-Seitz (WS) cell of volume  $V_{WS}$ . The NP is represented as a mesh of M vertices, where the ith vertex is associated with a surface charge  $q_i$ , position vector  $\vec{r}_i$ , and area element  $\mathcal{A}_i$ . The total surface charge of the discretized NP is  $Q = \sum_i^M q_i$ . The WS cell contains N monovalent counterions, which are present both inside and outside the NP. Assuming electroneutrality, we have Q = eN, where e is the electronic charge. Following the two-state Manning model approximation, we separate the counterions into  $\alpha N$  condensed ions and  $(1 - \alpha)N$  free ions, where  $\alpha$  represents the fraction of the

counterions that condense on the NP surface. The condensed ions are restricted to have translational motion in a thin shell surrounding the NP, while the free ions occupy the entire WS cell.

We archive the set of charges  $\{q_i\}$ , area elements  $\{\mathscr{A}_i\}$ , and position vectors  $\{\vec{r}_i\}$  associated with the M vertices specifying the shape of the NP produced at the end of the simulation. Using this data, we numerically extract the Coulomb energy  $\mathscr{U}$  of the discretized NP:

$$\mathscr{U} = \frac{l_B}{2} \sum_{i,i \neq j}^{M} \frac{q_i q_j}{|\vec{r}_i - \vec{r}_j|} + \sum_{i}^{M} \mathscr{U}_i^{\text{self}}, \tag{2}$$

where  $\mathscr{U}_i^{\text{self}} = l_B q_i^2 \sqrt{\pi/\mathscr{A}_i}$  is the Coulomb self-energy associated with the *i*th vertex, and  $\mathscr{U}$  is in units of  $k_B T$ . For large M, the simulation-derived estimate  $\mathscr{U}_s$  for a uniformly charged spherical NP of charge Q and radius R approaches the exact result  $U_s = l_B Q^2 / 2R$ .

When the NP undergoes a deformation away from the initial spherical conformation, the vertex charges  $\{q_i\}$  remain the same as that of the undeformed sphere. We assume that condensed counterions reduce the charge of all vertices by the same factor, resulting in the renormalized NP total charge of  $\sum_{i}^{M} (1 - \alpha)q_i = (1 - \alpha)Q$ . Following Eq. (2), the associated renormalized Coulomb energy becomes  $(1 - \alpha)^2 \mathcal{U}$ . Using this result in the standard Manning model, we write the free

energy of the NP-counterion system in units of  $k_BT$  as

$$\mathcal{F} = (1 - \alpha)^2 \mathcal{U} + \mathcal{H}^{\text{elastic}} + \alpha N \ln \left( \frac{\alpha N \Lambda^3}{\omega b} \right) - \alpha N$$
$$+ (1 - \alpha) N \ln \left[ \frac{(1 - \alpha) N \Lambda^3}{V_{\text{WS}}} \right] - (1 - \alpha) N. \tag{3}$$

The first and second terms are, respectively, the renormalized Coulomb energy and the elastic energy of the discretized NP of a given shape, area  $\mathscr{A} = \sum_{i}^{M} \mathscr{A}_{i}$ , and volume  $\mathscr{V}$ . The next two terms represent the entropy of the  $\alpha N$  condensed ions that move in a thin layer of volume  $\mathcal{A}b$  surrounding the NP, where b is the layer thickness. Following our earlier work [37,40], we assume a uniformly thick layer and approximate b as the Gouy-Chapman length  $\mathcal{A}/(2\pi l_B Q)$ . The last two terms correspond to the entropy of the  $(1 - \alpha)N$  free ions that occupy the WS cell of volume  $V_{WS}$  which is set by choosing the NP volume packing fraction  $\eta = \mathcal{V}/V_{\text{WS}}$ . A is the thermal de Broglie wavelength. Note that  $\mathscr{H}^{\text{elastic}}$  is extracted numerically, and it does not depend on  $\alpha$ . Further, the volume constraint enforces  $\mathcal{V} \approx \mathcal{V}_s$ , where  $\mathcal{V}_s$  is the volume of the initial, spherical NP. We note that replacing the simulation-derived quantities  $\mathcal{U}$ ,  $\mathscr{A}$ , and  $\mathscr{V}$  by the analytical expressions for the Coulomb energy, area, and volume of the NP, respectively, the free energy  $\mathscr{F}$  reduces to the free energy employed in our earlier Manning model [40].

The minimization of the free energy  $\mathscr{F}$  with respect to  $\alpha$  yields the extremum condition:

$$-2(1-\alpha)\mathcal{U} + N\ln\left(\frac{\alpha}{1-\alpha}\frac{1}{\eta}\frac{2\pi l_B Q^{\mathcal{V}}}{\mathscr{A}^2}\right) = 0. \quad (4)$$

We solve Eq. (4) using the built-in FindRoot function in Mathematica [53] to obtain the condensate fraction  $\alpha$  as a function of  $\eta$  for a discretized NP of a given shape,  $\mathcal{U}$ ,  $\mathcal{A}$ ,  $\mathcal{V}$ , and Q. Using  $\alpha$ , we evaluate the reduced effective charge

$$Q^{\text{eff}} = (1 - \alpha)Q \tag{5}$$

and the free energy of the NP following Eq. (3). The difference  $\Delta \mathscr{F} = \mathscr{F} - \mathscr{F}_s$  between the free energy  $\mathscr{F}$  of a deformed NP and the free energy  $\mathscr{F}_s$  of the associated undeformed spherical NP is given by

$$\Delta \mathscr{F} = (1 - \alpha^2) \mathscr{U} - (1 - \alpha_s^2) \mathscr{U}_s + N \ln \left( \frac{1 - \alpha}{1 - \alpha_s} \right) + \Delta \mathscr{H}^{\text{elastic}}, \tag{6}$$

where  $\alpha$  is the fraction of condensed ions on the surface of the deformed NP,  $\alpha_s$  is the corresponding condensate fraction for the initial, undeformed spherical NP, and  $\mathcal{U}$  and  $\mathcal{U}_s$  are respectively the Coulomb energies of the deformed NP and the spherical NP computed using Eq. (2). The last term  $\Delta \mathcal{H}^{\text{elastic}} = \mathcal{H}^{\text{elastic}} - \mathcal{H}^{\text{elastic}}_s$  is the difference between the elastic energies of the deformed NP and the spherical NP.

It is instructive to compare the predictions of the simulation-based approach with the results derived using the analytical Manning model calculations for cases where exact analytical expressions for the Coulomb energy of the deformed NPs are available. We consider a fully charged spherical NP characterized with R=20 nm,  $Q\approx 600e$ ,  $\kappa_b=5k_BT$ , and  $\kappa_s=125k_BT$ , and the associated deformed,

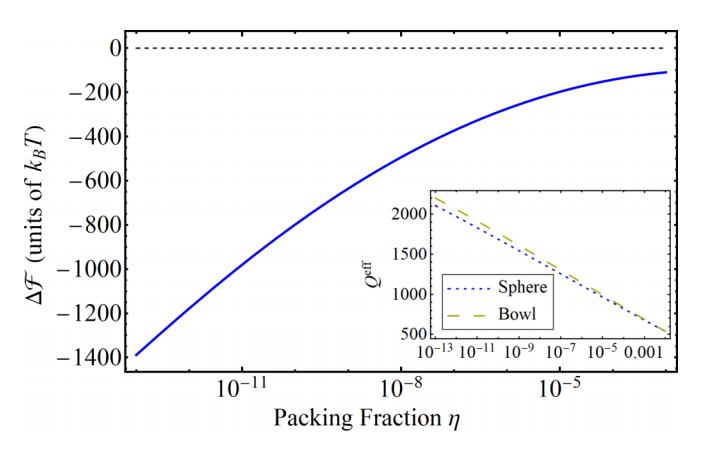


FIG. 6. Manning model results for the free-energy difference  $\Delta\mathscr{F}$  between a bowl-shaped NP realized in simulations (Fig. 1, top row, third snapshot from the left) and the undeformed spherical NP of radius R=50 nm. Both NPs have the same elastic moduli and surface charge Q=2513e in the dilute limit (packing fraction  $\eta \to 0$ ). Inset shows that the effective surface charges  $Q^{\rm eff}$  in units of e on the bowl (long yellow dashes) and sphere (small blue dashes) decrease with increasing  $\eta$ . The sphere-to-bowl shape transition is free-energetically favored ( $\Delta\mathscr{F} < 0$ ) for  $\eta$  up to  $10^{-2}$ .

disk-shaped NP (see the Appendix). We compute  $Q^{\rm eff}$  and  $\Delta\mathscr{F}$  associated with this sphere-to-disk transition using the simulation-informed Manning model via Eqs. (5) and (6), respectively. In our previous paper [40], we approximated the disk-shaped NP as a uniformly charged oblate spheroid of aspect ratio  $\lambda \approx 0.28$ , and used its analytically available Coulomb energy in a Manning model to evaluate the effective charges and the free energies of the sphere and the oblate spheroid. Figure 10 in the Appendix shows that  $Q^{\rm eff}$  and  $\Delta\mathscr{F}$  are in good agreement with the results obtained using the analytical approach for  $10^{-13} < \eta < 10^{-2}$ .

We now extract the effective charges and free-energy changes associated with the sphere-to-bowl shape transitions shown in Fig. 1 (top row). Transitions to two fully charged bowl-shaped NPs are considered to illustrate different scenarios. We first examine the free-energetic drive for a spherical NP of radius R = 50 nm to deform into a bowl-shaped NP realized at  $c_s = 0.1$  mM (Fig. 1, top row, third snapshot from the left). Condensate fractions  $\alpha$  and  $\alpha_s$  for the bowl-shaped NP and the spherical NP respectively are extracted by solving Eq. (4) for packing fraction  $\eta \in (10^{-13}, 10^{-2})$ . Figure 6 (inset) shows the corresponding effective surface charges  $Q^{\text{eff}} =$  $(1 - \alpha)Q$  and  $Q_s^{\text{eff}} = (1 - \alpha_s)Q$  [computed using Eq. (5)] on the bowl-shaped and spherical NPs, respectively. Deformed NP has a higher effective charge compared to the spherical NP for all  $\eta$ .  $Q^{\text{eff}}$  and  $Q_s^{\text{eff}}$  decrease with increasing  $\eta$  and large counterion condensation is observed at high  $\eta$  (e.g., for  $\eta = 10^{-2}$ ,  $Q^{\rm eff} \approx 539e$  and  $Q_s^{\rm eff} \approx 538e$ ). Figure 6 shows the difference  $\Delta \mathscr{F}$  [extracted using Eq. (6)] between the free energy of the deformed bowl-shaped NP and that of the undeformed spherical NP as a function of  $\eta$ .  $\Delta \mathscr{F} < 0$  for  $\eta$  up to  $10^{-2}$ , implying that the deformation to the bowl-shaped NP remains energetically favorable despite significant counterion condensation.

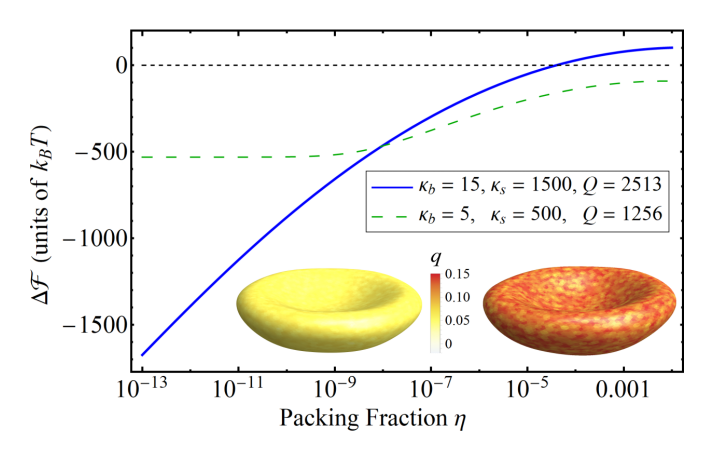


FIG. 7. Manning model results (solid blue line) for the free-energy difference  $\Delta \mathscr{F}$  associated with the deformation of a spherical NP of elastic moduli  $\kappa_b = 15k_BT$ ,  $\kappa_s = 1500k_BT$ , and surface charge Q = 2513e into a bowl-shaped NP (right snapshot in the inset). The deformation is free-energetically unfavorable ( $\Delta \mathscr{F} > 0$ ) for large packing fraction  $\eta > 10^{-4}$ . However, the deformation of a softer spherical NP ( $\kappa_b = 5k_BT$ ,  $\kappa_s = 500k_BT$ , Q = 1256e) into a similar bowl shape (left snapshot in the inset) under the same solution conditions is free-energetically favored (dashed green line) for  $\eta < 10^{-2}$ . The color bar indicates the charge in units of e associated with the vertices discretizing the NP surface.

We next examine the sphere-to-bowl shape transition realized at  $c_s = 0.05$  mM (Fig. 1, top row, second snapshot from the left). We find significant counterion condensation for both deformed and undeformed NPs at high  $\eta$  (e.g., for  $\eta = 10^{-2}$ ,  $Q^{\rm eff} \approx 542e$  and  $Q_{\rm s}^{\rm eff} \approx 538e$ ). The solid blue line in Fig. 7 shows the difference  $\Delta \mathscr{F}$  between the free energy of the deformed bowl-shaped NP and that of the undeformed spherical NP as a function of the packing fraction  $\eta$ . The deformation to this bowl-shaped NP becomes free-energetically unfavorable  $(\Delta \mathscr{F} > 0)$  for  $\eta \gtrsim 10^{-4}$ . The free-energetic drive for spherical NPs to deform into bowl shaped NPs can be reinstated at larger  $\eta$  by synthesizing softer NPs and tuning the total surface charge Q. For example, by reducing the NP elastic moduli to  $\kappa_b = 5k_BT$ ,  $\kappa_s = 500k_BT$  and lowering the surface charge to Q = 1256e (charge density  $\sigma = 0.04e/\text{nm}^2$ ), simulations reveal a transition to a bowl-shaped NP of similar area (left snapshot in the inset of Fig. 7). The difference between the free energy of this bowl-shaped NP and that of the associated spherical NP (dashed green line) is negative for all  $\eta \in (10^{-13}, 10^{-2})$ . Figure 11 in the Appendix shows that these softer NPs also deform as a result of changes in charge coverage, yielding shapes similar to those observed in Fig. 1 (second column from the left).

Our Manning model-based analysis employs many approximations. The counterion distribution around the deformed NP surface is assumed isotropic, which is an oversimplification for shapes that deviate significantly from the spherical conformation. The free energy does not include the energy associated with counterion-counterion Coulomb interactions. Further, the deformed NP is placed in a counterion-only environment that is free of salt ions. More quantitative results that address some of these simplifications can be obtained by adopting a more rigorous approach such as

the Poisson-Boltzmann (PB) theory. However, solutions of the PB differential equation for the nonspherical conformations characterizing the deformed NPs are difficult to obtain without making simplified approximations such as treating the NPs as ideal spheroids or concave bowls. Adopting a more phenomenological model such as the Manning two-state model enables us to incorporate information (e.g., Coulomb energy, area) directly related to the deformed NPs realized in simulations for extracting the NP effective charge and free energy.

We note that the effects arising from explicit counterion-NP interactions during the shape change process are neglected in our deformable NP model system, but can become important. For example, a significant release of counterions into the bulk as the NP deforms may increase the net free energy of the released ions and stabilize the spherical NP [54]. These effects may affect the parameter regimes to realize shape transitions, in particular, for higher NP packing fractions.

## IV. CONCLUSION

We have studied the deformations that can be engineered in spherical NPs of radius R=50 nm, bending modulus  $\kappa_b=15k_BT$ , and stretching modulus  $\kappa_s=1500k_BT$  by designing the NP surface with octahedrally distributed charged patches and double-cap charged patches characterized with surface charge density  $\sigma\approx 0.08e/\text{nm}^2$ . We find the lowenergy shapes of these deformable charge-patterned NPs by minimizing a coarse-grained model Hamiltonian that captures the NP elastic and electrostatic energies. The minimization is performed subject to a volume constraint using an MD-based simulated annealing method. The low-energy NP shape changes with the type of charge pattern, fractional surface charge coverage, and salt concentration.

Spherical NPs designed with octahedrally distributed charged patches deform into rounded octahedra, faceted octahedra, faceted bowls, and rounded bowls of different depths in response to changes in charge coverage and salt concentration over 0.01-10 mM. The same NPs when designed with double-cap charged patches deform into oblate spheroids, spherocylinders, and dented beans in response to similar changes in charge coverage and salt concentration. We demonstrate that similar shape transitions can be realized in deformable NPs of different sizes characterized with R=30 and 75 nm by tuning the NP design attributes and solution conditions. The deformations, controlled by pattern type and screening length, can change the directional specificity of interactions between NPs, which may hinder or promote reconfiguration in assembled materials.

All shape transitions are accompanied by a rise in the NP surface area, which is driven by the electrostatic repulsion between charged moieties. Deformed NPs have lower electrostatic and total energy compared to the associated spherical NPs. Further, the elastic and electrostatic energy densities on the surface of the deformed NPs are inhomogeneous and coupled to the NP shape.

We note the similarities between some of the low-energy NP shapes shown in Figs. 1 and 2, and the low-energy shapes of larger, micron-size fluid membrane vesicles [55] described via a "minimal model" Hamiltonian characterized

with only the bending energy term in Eq. (1). By minimizing the bending energy under both area and volume constraints, transitions to oblate and prolate spheroids, biconcave discocytes, dumbbell-type structures, and bowl-shaped stomatocytes were observed with decreasing vesicle volume  $\mathcal{V}$  [55]. Vesicles of these different shapes have the same area  $\mathcal{A}$  and are characterized with a single dimensionless parameter: the reduced volume  $v = \mathcal{V}/[(4\pi/3)\mathcal{R}^3]$ , where  $\mathcal{R}$  is the radius of the spherical vesicle of area  $\mathcal{A}$ .

The similarities between some shapes of vesicles and NPs can be understood in a qualitative way by interpreting the competition between the electrostatic and stretching energies as setting up an effective area constraint. This constraint yields an NP area A which depends on the charge pattern type, the extent of the surface charge coverage p, and the salt concentration  $c_s$ . For p > 0, the deformed NP has an area A greater than the area  $A_s$  of the spherical NP of radius R (Fig. 3), but shares the same volume  $\mathcal{V} = (4\pi/3)R^3$  due to the imposed volume constraint. This yields a reduced volume  $v = \mathcal{V}/[(4\pi/3)\mathcal{R}^3] < 1$ , where  $\mathcal{R} > R$  is the radius of the sphere of area A. Larger NP areas resulting from lower  $c_s$ or higher p yield smaller v. Thus, the problem of finding the volume-preserving, energetically favorable deformations of charged NPs described by the Hamiltonian in Eq. (1) can be transformed into a problem of minimizing the bending energy of uncharged NPs for different reduced volumes  $v \in (0, 1)$ , subject to an effective area constraint and a volume constraint. In the uncharged limit of  $p \to 0$ , the stretching energy constrains the NP area to  $A_s$ , yielding  $v \approx 1$  for which the shape that minimizes the bending energy is a sphere, in agreement with our observations. As v decreases, the NP shape that minimizes the bending energy shifts, yielding shapes similar to those observed in the studies of the large, uncharged vesicles [55].

Despite the similarities in the shapes, the control mechanisms underlying the shape transitions in these uncharged vesicles are different from those associated with the electrostatics-based shape control of the flexible charge-patterned NPs. There are also differences in the implementation of the geometric constraints, e.g., only the volume constraint is enforced during the NP deformation. Further, the effects of the coupling between surface charge patterns and the low-energy NP shapes, as evidenced by the inhomogeneous elastic and electrostatic energy densities on the NP surface (Figs. 5 and 9), are entirely absent in the homogeneous vesicles.

To assess the stability of shape transitions for nondilute conditions where counterion condensation effects may become important, we develop a Manning model that utilizes simulation-derived estimates for the NP Coulomb energy to extract the free energy associated with the deformation of fully charged spherical NPs into bowl-shaped NPs. Transitions are found to be free-energetically favorable for many bowl-shaped NPs over a wide range of NP packing fraction  $\eta \in (10^{-13}, 10^{-2})$ . In some cases involving high  $\eta > 10^{-4}$ , where counterion condensation is significant to inhibit deformation, the free-energetic drive to deform can be restored by synthesizing softer NPs. The simulation-informed Manning model can be used to evaluate ion condensation effects for NPs characterized with complex

shapes for which the electrostatic energy is not available analytically.

During the assembly of many flexible NPs, the interactions between NPs can generate perturbations around the low-energy shapes observed here, which in turn can alter the assembly kinetics. The shape fluctuations of a NP in response to its local environment will depend on the NP packing fraction, NP flexibility, and the shape-switching protocol followed. Similar to the previous simulation-based studies of shape-changing nanorods [6] and deformable colloids [2], we expect the assembly of multiple deformable patchy NPs to exhibit effects of shape and size polydispersity. As these studies show, the assembly pathways to ordered structures can be tailored to be robust in the presence of such shape fluctuations, yielding transitions to new ordered structures with stable long-range order nucleated by a shift in the average shape of the building blocks [2].

We realize that a key experimental challenge will be to synthesize deformable NPs with tailored charge patterns. Phase separation and masking techniques are established methods for synthesizing polymer-based patchy particles [28], which may be utilized with pH-responsive polymers to form charge-patterned NPs [9,28]. The deformation can be facilitated by controlling the extent of crosslinking in polymeric NPs [10,11], which can tune the NP elasticities to values within the range of elastic moduli explored in this work. For example, hydrogel NPs with Young's modulus in the range of 18–211 kPa have been synthesized by changing the crosslinker polymer concentration [11]. Further, recent experiments show that nanogel particles of radius 50–150 nm characterized with elastic moduli within 30–71 kPa deform significantly away from the spherical shape [10,49].

## ACKNOWLEDGMENTS

This work is supported by the National Science Foundation through Grants No. DMR-1753182 and No. 1720625. Simulations were performed using the Big Red supercomputing systems. N.E.B. contributed to this work prior to his employment with American Regent.

## APPENDIX: SUPPLEMENTARY RESULTS

Figure 8 shows that tuning NP elasticity has a significant effect on the low-energy shapes of charge-patterned deformable NPs. The bottom row reproduces the low-energy shapes shown in Fig. 1 (second column from the right) for NPs patterned with octahedrally distributed charged patches that have bending modulus  $\kappa_b = 15k_BT$  and stretching modulus  $\kappa_s = 1500k_BT$ . At a salt concentration of  $c_s = 1$  mM, these NPs deform into rounded octahedra and bowls as the charge coverage p is increased from 0.25 to 1. The top row shows the low-energy shapes observed for the same NPs when their stretching modulus is lowered to  $\kappa_s = 375k_BT$  (all other NP features and solution conditions are kept the same). As the charge coverage p is increased from 0.25 to 1, these softer NPs deform into rounded cubes, faceted plates, and flattened round bowls.

In the main text, we introduce a Manning model that utilizes simulation-informed estimates for the energy and geometrical properties of the deformed NP to extract the free

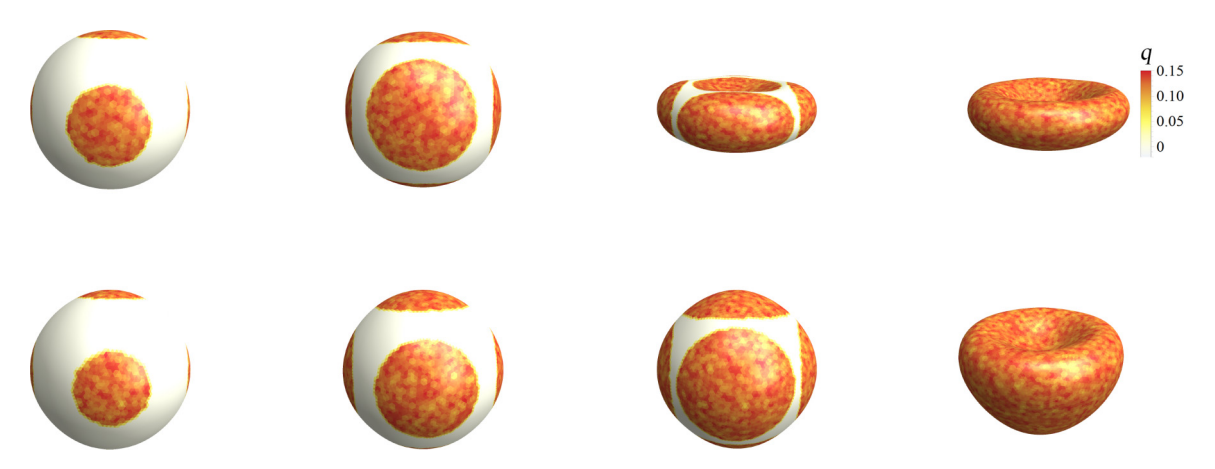


FIG. 8. Low-energy shapes of deformable NPs of stretching modulus  $\kappa_s = 375k_BT$  (top row) and  $\kappa_s = 1500k_BT$  (bottom row). NPs are patterned with octahedrally distributed charged patches (colored in orange) and have a surface charge of pQ, where  $Q \approx 2513e$  is the total charge associated with a fully charged NP and p is the fractional charge coverage parameter increasing from left to right as 0.25, 0.50, 0.75, 1.0. The color bar indicates the charge in units of e associated with the vertices discretizing the NP surface. All NPs have the same bending modulus  $\kappa_b = 15k_BT$ , volume  $\approx (4/3)\pi 50^3$  nm<sup>3</sup> and are in a salt solution of concentration  $c_s = 1$  mM. Tuning NP elasticity has a significant effect on the shape transitions exhibited by these charge-patterned deformable NPs.

energy associated with the NP deformation in the presence of counterions. Here we test this simulation-informed approach by comparing its predictions with the analytical Manning model calculations performed in our earlier work for the sphere-to-disk shape transition observed for a fully charged spherical NP characterized with R = 20 nm,  $Q \approx 600e$ ,  $\kappa_b = 5k_BT$ , and  $\kappa_s = 125k_BT$  [40]. The analytical Manning model

was validated using explicit-ion MD simulations at packing fractions  $\eta=10^{-3}, 10^{-2}$ . Following our previous paper, we approximate the disk-shaped NP as a uniformly charged oblate spheroid of aspect ratio  $\lambda\approx 0.28$  and use an exact analytical expression for its Coulomb energy and area to write the free energy of the NP-counterion system [37,40]. Figure 10 shows that the effective charges (inset) and the

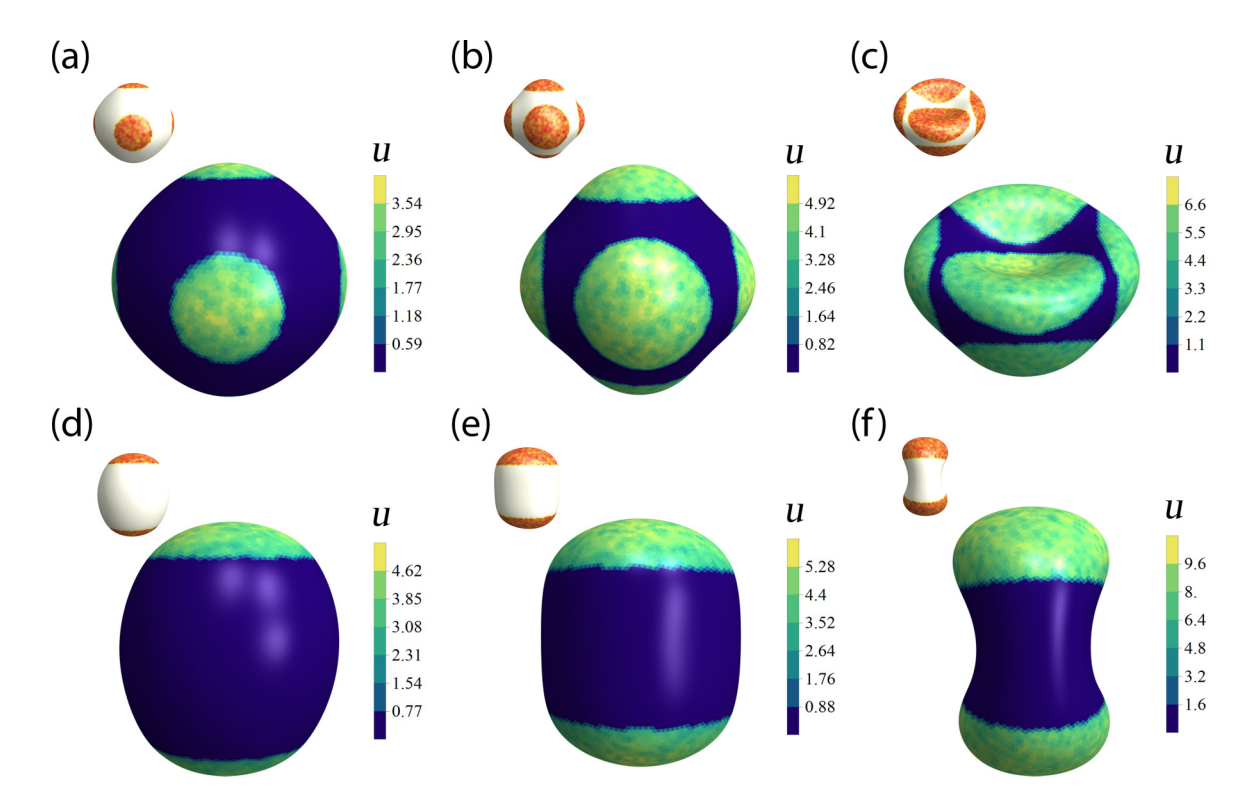


FIG. 9. The electrostatic energy density u in units of  $k_BT$  for the representative set of deformed NPs shown in Fig. 5. NPs are tailored with octahedrally distributed charged patches characterized by charge coverage p = 0.25 (a), p = 0.5 (b), p = 0.75 (c), and double-cap patterns characterized by p = 0.25 (d), p = 0.4 (e), and p = 0.5 (f). The top left image in each case shows the associated surface charge pattern. The electrostatic energy density is inhomogeneous and exhibits a strong coupling to the surface charge pattern.

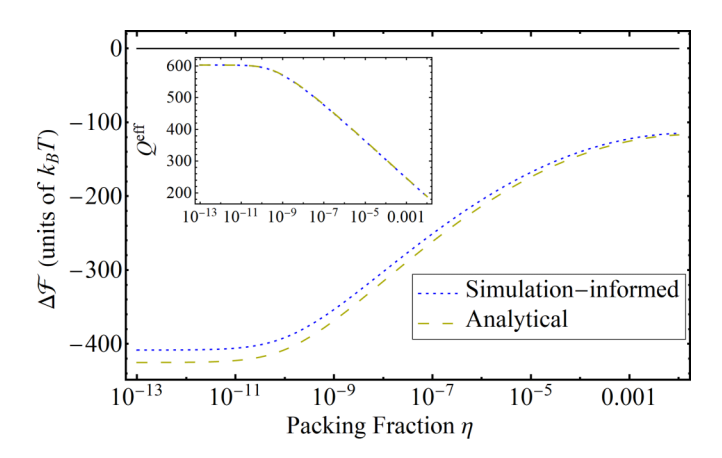


FIG. 10. Free-energy difference between a fully charged disk-shaped NP and a spherical NP of radius R = 20 nm, surface charge  $Q \approx 600e$ , and elastic moduli  $\kappa_b = 5k_BT$ ,  $\kappa_s = 125k_BT$  obtained using simulation-informed (small blue dashes) and analytical Manning model calculations (large yellow dashes). Inset shows the effective surface charges  $Q^{\text{eff}}$  in units of e on the disk-shaped NP extracted using the two approaches. The simulation-informed Manning model results are in good agreement with the analytical Manning model results, and both show that sphere-to-disk shape transition is free-energetically favored for packing fraction  $\eta$  up to  $10^{-2}$ .

free-energy differences extracted via the simulation-informed Manning model using Eqs. (5) and (6) are in good agreement with the results obtained using the analytical approach for  $10^{-13} < \eta < 10^{-2}$ .

In the main text, we showed that softer NPs characterized with  $\kappa_b = 5k_BT$ ,  $\kappa_s = 500k_BT$  and  $\sigma = 0.04e/\text{nm}^2$  exhibit a free-energetically favorable drive to deform into

bowl-shaped NPs when fully charged (Fig. 7). Figure 11 shows that these NPs also deform in response to changing charge coverage of octahedrally distributed charged patches at salt concentration  $c_s = 0.05$  mM, yielding shapes similar to those shown in Fig. 1 (second column from the left), including rounded octahedra, faceted octahedra, and faceted bowls.









FIG. 11. NPs designed with octahedrally distributed patches and characterized with elastic moduli  $\kappa_b = 5k_BT$ ,  $\kappa_s = 500k_BT$  yield low-energy shapes similar to those shown in Fig. 1 (second column from the left) at salt concentration 0.01 mM. NPs have a surface charge of pQ, where  $Q \approx 1256e$  is the total charge associated with a fully charged NP. Charge coverage increases from left to right as p = 0.25, 0.50, 0.75, 1.0. The color bar indicates the charge in units of e associated with the vertices discretizing the NP surface.

- [1] T. D. Nguyen, E. Jankowski, and S. C. Glotzer, Self-assembly and reconfigurability of shape-shifting particles, ACS Nano 5, 8892 (2011).
- [2] V. M. O. Batista and M. A. Miller, Crystallization of Deformable Spherical Colloids, Phys. Rev. Lett. 105, 088305 (2010).
- [3] O. Gang and Y. Zhang, Shaping phases by phasing shapes, ACS Nano 5, 8459 (2011).
- [4] Y. Zhang, F. Lu, D. van der Lelie, and O. Gang, Continuous Phase Transformation in Nanocube Assemblies, Phys. Rev. Lett. 107, 135701 (2011).
- [5] K. Bian, J. J. Choi, A. Kaushik, P. Clancy, D.-M. Smilgies, and T. Hanrath, Shape-anisotropy driven symmetry transformations in nanocrystal superlattice polymorphs, ACS Nano 5, 2815 (2011).
- [6] T. D. Nguyen and S. C. Glotzer, Reconfigurable assemblies of shape-changing nanorods, ACS Nano 4, 2585 (2010).

- [7] R. L. Marson, T. D. Nguyen, and S. C. Glotzer, Rational design of nanomaterials from assembly and reconfigurability of polymer-tethered nanoparticles, MRS Commun. 5, 397 (2015).
- [8] N. Tanjeem, D. M. Hall, M. B. Minnis, R. C. Hayward, and G. M. Grason, Focusing frustration for self-limiting assembly of flexible, curved particles, Phys. Rev. Res. 4, 033035 (2022).
- [9] D. Klinger, C. X. Wang, L. A. Connal, D. J. Audus, S. G. Jang, S. Kraemer, K. L. Killops, G. H. Fredrickson, E. J. Kramer, and C. J. Hawker, A facile synthesis of dynamic, shape-changing polymer particles, Angew. Chem., Int. Ed. 53, 7018 (2014).
- [10] J. W. Myerson, B. Braender, O. Mcpherson, P. M. Glassman, R. Y. Kiseleva, V. V. Shuvaev, O. Marcos-Contreras, M. E. Grady, H.-S. Lee, C. F. Greineder *et al.*, Flexible nanoparticles reach sterically obscured endothelial targets inaccessible to rigid nanoparticles, Adv. Mater. 30, 1802373 (2018).
- [11] X. Banquy, F. Suarez, A. Argaw, J.-M. Rabanel, P. Grutter, J.-F. Bouchard, P. Hildgen, and S. Giasson, Effect of

- mechanical properties of hydrogel nanoparticles on macrophage cell uptake, Soft Matter **5**, 3984 (2009).
- [12] C. Chen, R. A. Wylie, D. Klinger, and L. A. Connal, Shape control of soft nanoparticles and their assemblies, Chem. Mater. 29, 1918 (2017).
- [13] N. S. Abadeer and C. J. Murphy, Recent progress in cancer thermal therapy using gold nanoparticles, J. Phys. Chem. C 120, 4691 (2016).
- [14] Y. Liu, J. Tan, A. Thomas, D. Ou-Yang, and V. R. Muzykantov, The shape of things to come: importance of design in nanotechnology for drug delivery, Therapeu. Deliv. 3, 181 (2012).
- [15] K. Zhou, Y. Wang, X. Huang, K. Luby-Phelps, B. D. Sumer, and J. Gao, Tunable, ultrasensitive ph-responsive nanoparticles targeting specific endocytic organelles in living cells, Angew. Chem., Int. Ed. 50, 6109 (2011).
- [16] N. Shimokawa, H. Ito, and Y. Higuchi, Coarse-grained molecular dynamics simulation for uptake of nanoparticles into a charged lipid vesicle dominated by electrostatic interactions, Phys. Rev. E 100, 012407 (2019).
- [17] D. B. Chithrani, Intracellular uptake, transport, and processing of gold nanostructures, Molec. Membr. Biol. 27, 299 (2010).
- [18] S. Nangia and R. Sureshkumar, Effects of nanoparticle charge and shape anisotropy on translocation through cell membranes, Langmuir 28, 17666 (2012).
- [19] L. Chen, X. Li, Y. Zhang, T. Chen, S. Xiao, and H. Liang, Morphological and mechanical determinants of cellular uptake of deformable nanoparticles, Nanoscale 10, 11969 (2018).
- [20] A. P. Blum, J. K. Kammeyer, A. M. Rush, C. E. Callmann, M. E. Hahn, and N. C. Gianneschi, Stimuli-responsive nanomaterials for biomedical applications, J. Am. Chem. Soc. 137, 2140 (2015).
- [21] J.-W. Yoo and S. Mitragotri, Polymer particles that switch shape in response to a stimulus, Proc. Natl. Acad. Sci. USA 107, 11205 (2010).
- [22] F. Checot, S. Lecommandoux, H.-A. Klok, and Y. Gnanou, From supramolecular polymersomes to stimuli-responsive nano-capsules based on poly (diene-b-peptide) diblock copolymers, Eur. Phys. J. E 10, 25 (2003).
- [23] K. E. Gebhardt, S. Ahn, G. Venkatachalam, and D. A. Savin, Rod-sphere transition in polybutadiene- poly (l-lysine) block copolymer assemblies, Langmuir 23, 2851 (2007).
- [24] T. Wu, H. Sun, J. Jiang, S. Lin, L. Fan, K. Hong, Q. Sun, Y. Hu, Y. Zhu, and J. Du, Homopolymer nanobowls with a controlled size and denting degree, Polym. Chem. 13, 1236 (2022).
- [25] P. l. van Oostrum, M. Hejazifar, C. Niedermayer, and E. Reimhult, Simple method for the synthesis of inverse patchy colloids, J. Phys.: Condens. Matter 27, 234105 (2015).
- [26] F. Chang, B. G. Van Ravensteijn, K. S. Lacina, and W. K. Kegel, Bifunctional janus spheres with chemically orthogonal patches, ACS Macro Lett. 8, 714 (2019).
- [27] Y. Yi, L. Sanchez, Y. Gao, and Y. Yu, Janus particles for biological imaging and sensing, Analyst 141, 3526 (2016).
- [28] M. Lattuada and T. A. Hatton, Synthesis, properties and applications of janus nanoparticles, Nano Today 6, 286 (2011).
- [29] C. Gao, S. Kewalramani, D. M. Valencia, H. Li, J. M. McCourt, M. Olvera de la Cruz, and M. J. Bedzyk, Electrostatic shape control of a charged molecular membrane from ribbon to scroll, Proc. Natl. Acad. Sci. USA 116, 22030 (2019).
- [30] N. E. Brunk, M. Uchida, B. Lee, M. Fukuto, L. Yang, T. Douglas, and V. Jadhao, Linker-mediated assembly of virus-like

- particles into ordered arrays via electrostatic control, ACS Appl. Bio Mater. **2**, 2192 (2019).
- [31] M. Uchida, N. E. Brunk, N. D. Hewagama, B. Lee, P. E. Prevelige Jr, V. Jadhao, and T. Douglas, Multilayered ordered protein arrays self-assembled from a mixed population of viruslike particles, ACS Nano 16, 7662 (2022).
- [32] J. Lidmar, L. Mirny, and D. R. Nelson, Virus shapes and buckling transitions in spherical shells, Phys. Rev. E 68, 051910 (2003).
- [33] G. A. Vliegenthart and G. Gompper, Compression, crumpling and collapse of spherical shells and capsules, New J. Phys. 13, 045020 (2011).
- [34] E. H. Yong, D. R. Nelson, and L. Mahadevan, Elastic Platonic Shells, Phys. Rev. Lett. 111, 177801 (2013).
- [35] H. Yuan and M. Olvera de la Cruz, Crystalline membrane morphology beyond polyhedra, Phys. Rev. E 100, 012610 (2019).
- [36] V. Jadhao, C. K. Thomas, and M. Olvera de la Cruz, Electrostatics-driven shape transitions in soft shells, Proc. Natl. Acad. Sci. USA 111, 12673 (2014).
- [37] V. Jadhao, Z. Yao, C. K. Thomas, and M. Olvera de la Cruz, Coulomb energy of uniformly charged spheroidal shell systems, Phys. Rev. E **91**, 032305 (2015).
- [38] N. E. Brunk and V. Jadhao, Computational studies of shape control of charged deformable nanocontainers, J. Mater. Chem. B 7, 6370 (2019).
- [39] Z. Yao and M. Olvera de la Cruz, Electrostatics-Driven Hierarchical Buckling of Charged Flexible Ribbons, Phys. Rev. Lett. **116**, 148101 (2016).
- [40] N. E. Brunk, J. Kadupitiya, and V. Jadhao, Designing Surface Charge Patterns for Shape Control of Deformable Nanoparticles, Phys. Rev. Lett. 125, 248001 (2020).
- [41] G. Vernizzi, R. Sknepnek, and M. Olvera de la Cruz, Platonic and archimedean geometries in multicomponent elastic membranes, Proc. Natl. Acad. Sci. USA 108, 4292 (2011).
- [42] J. Paulose and D. R. Nelson, Buckling pathways in spherical shells with soft spots, Soft Matter 9, 8227 (2013).
- [43] S. S. Datta, S.-H. Kim, J. Paulose, A. Abbaspourrad, D. R. Nelson, and D. A. Weitz, Delayed Buckling and Guided Folding of Inhomogeneous Capsules, Phys. Rev. Lett. 109, 134302 (2012).
- [44] R. Sknepnek and M. Olvera de la Cruz, Nonlinear elastic model for faceting of vesicles with soft grain boundaries, Phys. Rev. E **85**, 050501(R) (2012).
- [45] R. Sknepnek, G. Vernizzi, and M. Olvera de la Cruz, Shape change of nanocontainers via a reversible ionic buckling, Phys. Rev. Lett. **106**, 215504 (2011).
- [46] M. D. Emanuel, A. G. Cherstvy, R. Metzler, and G. Gompper, Buckling transitions and soft-phase invasion of two-component icosahedral shells, Phys. Rev. E 102, 062104 (2020).
- [47] C. Huang, P. J. Butler, S. Tong, H. S. Muddana, G. Bao, and S. Zhang, Substrate stiffness regulates cellular uptake of nanoparticles, Nano Lett. 13, 1611 (2013).
- [48] S. Zhang, H. Gao, and G. Bao, Physical principles of nanoparticle cellular endocytosis, ACS Nano 9, 8655 (2015).
- [49] P. Guo, D. Liu, K. Subramanyam, B. Wang, J. Yang, J. Huang, D. T. Auguste, and M. A. Moses, Nanoparticle elasticity directs tumor uptake, Nat. Commun. 9, 130 (2018).
- [50] S. E. Gratton, P. A. Ropp, P. D. Pohlhaus, J. C. Luft, V. J. Madden, M. E. Napier, and J. M. DeSimone, The effect of

- particle design on cellular internalization pathways, Proc. Natl. Acad. Sci. USA **105**, 11613 (2008).
- [51] Code available at https://github.com/softmaterialslab/np-shape-lab/. Associated simulation tool available online at https://nanohub.org/tools/npshapelab.
- [52] J.-P. Ryckaert, G. Ciccotti, and H. J. C. Berendsen, Numerical integration of the cartesian equations of motion of a system with
- constraints: Molecular dynamics of n-alkanes, J. Comput. Phys. **23**, 327 (1977).
- [53] W. R. Inc., Mathematica, Version 12.1, Champaign, IL (2020).
- [54] Y. Jho, J. Landy, and P. Pincus, Charge renormalization for ellipsoidal macroions, ACS Macro Lett. **4**, 640 (2015).
- [55] U. Seifert, Configurations of fluid membranes and vesicles, Adv. Phys. **46**, 13 (1997).